

Robust Reconstruction of Fluorescence Molecular Tomography Based on Sparsity Adaptive Correntropy Matching Pursuit Method for Stem Cell Distribution

Shuai Zhang, Xibo Ma, Yi Wang, Meng Wu, Hui Meng, Wei Chai, Xiaojie Wang,
Shoushui Wei, and Jie Tian[✉], *Fellow, IEEE*

Abstract—Fluorescence molecular tomography (FMT), as a promising imaging modality in preclinical research, can obtain the three-dimensional (3-D) position information of the stem cell in mice. However, because of the ill-posed nature and sensitivity to noise of the inverse problem, it is a challenge to develop a robust reconstruction method, which can accurately locate the stem cells and define the distribution. In this paper, we proposed a sparsity adaptive correntropy matching pursuit (SACMP) method. SACMP method is independent on the noise distribution of measurements and it assigns small weights on severely corrupted entries of data and large weights on clean ones adaptively. These properties make it more suitable for *in vivo* experiment. To analyze the performance in terms of robustness and practicability of SACMP, we conducted numerical simulation and *in vivo* mice experiments. The results demonstrated

Manuscript received January 6, 2018; revised March 31, 2018; accepted April 2, 2018. Date of publication April 9, 2018; date of current version October 1, 2018. This work was supported in part by the National Key Research Program of China under Grant 2016YFA0100900, Grant 2016YFA0100902, and Grant 2017YFA0205200, in part by the National Natural Science Foundation of China under Grant 81227901, Grant 815270805, Grant 61231004, Grant 81471739, Grant 81472594, and Grant 81770781, and in part by the Scientific Research and Equipment Development Project of Chinese Academy of Sciences under Grant YZ201457. (*Shuai Zhang and Xibo Ma contributed equally to this work.*) (*Corresponding authors: Xibo Ma; Shoushui Wei; Jie Tian.*)

S. Zhang is with the Institute of Biomedical Engineering, School of Control Science and Engineering, Shandong University, Jinan 250061, China, and also with the CAS Key Laboratory of Molecular Imaging, Institute of Automation, Chinese Academy of Sciences, Beijing 100190, China (e-mail: zhangs@mail.sdu.edu.cn).

X. Ma, H. Meng, and J. Tian are with the CAS Key Laboratory of Molecular Imaging, Institute of Automation, Beijing 100190, China, also with the Beijing Key Laboratory of Molecular Imaging, Beijing 100190, China, also with the State Key Laboratory of Management and Control for Complex Systems, Chinese Academy of Sciences, Beijing 100190, China, and also with the University of Chinese Academy of Sciences, Beijing 100049, China (e-mail: xibo.ma@ia.ac.cn; menghui2015@ia.ac.cn; tian@iee.org).

Y. Wang and W. Chai are with Chinese PLA General Hospital, Medical College of PLA, Beijing 100853, China (e-mail: wangyi@fingerpass.net.cn; chaiwei301@163.com).

M. Wu and X. Wang are with the School of Life Science, Ludong University, Yantai 264001, China (e-mail: wumeng@fingerpass.net.cn; wxj10304@126.com).

S. Wei is with the Institute of Biomedical Engineering, School of Control Science and Engineering, Shandong University, Jinan 250061, China (e-mail: sswei@sdu.edu.cn).

Color versions of one or more of the figures in this paper are available online at <http://ieeexplore.ieee.org>.

Digital Object Identifier 10.1109/TMI.2018.2825102

that the SACMP method obtained the highest robustness and accuracy in locating stem cells and depicting stem cell distribution compared with stagewise orthogonal matching pursuit and sparsity adaptive subspace pursuit reconstruction methods. To the best of our knowledge, this is the first study that acquired such accurate and robust FMT distribution reconstruction for stem cell tracking in mice brain. This promotes the application of FMT in locating stem cell and distribution reconstruction in practical mice brain injury models.

Index Terms—Fluorescence molecular tomography, inverse problem, sparsity adaptive correntropy matching pursuit, robust reconstruction.

I. INTRODUCTION

FLUORESCENCE molecular imaging can noninvasively monitor the stem cells migration, homing and differentiation by detecting the distribution of molecular probe [1]–[5]. However, two-dimensional (2D) surface fluorescence derived from the inner light sources of organisms after scattering and absorption, only provide the 2D qualitative information of stem cell aggregation, which does not reflect its 3D cluster morphology and distant effect. This severely limits its application for quantitatively stem cell tracking. Therefore, many research groups have devoted to developing fluorescence tomography systems and algorithms in order to reconstruct the 3D distribution of fluorescent probes [6]–[13]. This is an important technique with great potential for the study of stem cells, as there are not a definite interpretation for the mechanism and toxicity of stem cells in organisms in preclinical and clinical research [14], [15].

To reconstruct accurate FMT light source, FMI is typically acquired from different angles and fused with CT images so that anatomical structure can be used as the prior information to reduce the ill-posedness of inverse problem [11]. However, the problem still exist because noise introduced during data acquirement and discretization will severely influence the FMT reconstruction. Thus there are various challenges to reconstruct stem cell distribution in living organisms [10], [16]–[18].

One of the major solutions is proposed based on the assumption that fluorescent source is sparse, because the fluorescent probe distribution is relatively concentrated in some specific areas compared to the whole organ [18]. Many sparse methods under the assumption have been developed to improve the

quality of reconstruction results. Either sparse regularization terms (L_0 , L_1 , L_p etc.) [9], [18]–[20] or greedy strategies are used to ensure sparsity of solutions [21]–[23]. Although, the algorithms which explicitly adopt sparse-type regularization can locate the fluorescent source positions accurately, they usually require lots of iterations to get satisfactory results, especially when the dimension of the FMT inverse problem is considerable [24].

For the purpose of improving the FMT reconstruction efficiency, some researchers have consideration on the combination of sparse regularization and compressive sensing (CS) theory for FMT reconstruction [19], [20], [25]. Under the framework of the CS theory, the StOMP algorithm that incorporate greedy pursuit strategy has been used to solve the FMT inverse problem [21]. The method can usually achieve acceptable results after a little calculation time, while the sparsity factor need to be estimated in advance. However, for the FMT reconstruction problem in practical, sparsity factor is unknown and artificial estimation of it generally detract from the result accuracy. In response to this problem, a method based on SASP, which estimates and updates the sparsity adaptively using a bottom-up approach during the iterations, was proposed to be more suitable for practical biomedical research [23].

Most conventional matching pursuit (MP) methods estimate the target sparse vector through solving least squares problem under the mean square error (MSE) criterion. The prerequisite for MSE criterion is that the noise distribution conforms to the Gaussian assumption which largely limits the application of these methods [26]–[29]. In this study, we propose a SACMP method for stem cell distribution reconstruction. For SACMP method, correntropy induced metric (CIM) [27] of the residual is used instead of MSE for the target sparse vector estimation [30]. The method is agnostic to noise distribution and can handle on measurements with Gaussian and non-Gaussian noise for the FMT reconstruction. In addition, MP methods usually evaluate the correlation between residual and all atoms to select the target atoms. Once the measurements are disturbed by the noise, the selected atoms will be extremely inaccurate. To alleviate this limitation, we adopt the optimization algorithm based on half-quadratic (HQ) theory [31] to minimize the CIM of the residual and calculate the weight vector to improve the accuracy of the selected atoms.

In particular, there are some challenges in reconstructing stem cell distribution for FMT. The number of the stem cells in mice is fewer and the distribution is more dispersed, compared to tumor cells in tumor bearing mice. It is a multiple light sources reconstruction problem with low signal to noise ratio which resulting in hardly getting robust and accurate solutions. Therefore, it is necessary to develop a more robust and accurate reconstruction algorithm. And SACMP method is proved to alleviate the ill-posedness of the FMT inverse problem and have better performance on robustness and accuracy.

To evaluate the performance of SACMP method, numerical simulation experiments and *in vivo* experiments of stem cell distribution in brain injury mice were carried out. StOMP and SASP methods were used for comparison, and the anatomical

information derived from CT was applied to build the heterogeneous mouse model. The MRI results were considered to be the actual location and distribution of stem cells in mice and were used as reference of evaluation for all methods.

This paper is organized as follows: Section II introduces the photon propagation model (PPM), the linear relationship between inner fluorescence source and surface photon distribution, the reconstruction algorithm based on SACMP and the evaluation index. Section III describes the contents and results of numerical simulation experiments and *in vivo* stem cell distribution experiments. At last, Section IV presents discussion, conclusion and future application of our method.

II. METHODOLOGY

A. Photon Propagation Model and Inverse Problem of FMT

For the continuous-wave FMT of the point excitation sources, the photon propagation in the biological tissue within the near-infrared spectroscopy window can be described by a pair of coupled diffusion equations, plus the Robin-type boundary condition, which can be expressed as follows [7]:

$$\left\{ \begin{array}{l} \nabla [D_x(r) \nabla \Phi_x(r)] - \mu_{ax}(r) \Phi_x(r) \\ \quad = -\Theta \delta(r - r_l) (r \in \Omega) \\ \nabla [D_m(r) \nabla \Phi_m(r)] - \mu_{am}(r) \Phi_m(r) \\ \quad = -\Phi_x(r) \eta \mu_{af}(r) (r \in \Omega) \\ 2D_{x,m}(r) \nabla \Phi_{x,m}(r) + q \Phi_{x,m}(r) = 0 (r \in \partial\Omega) \end{array} \right. \quad (1)$$

where r denotes the nodes inside the problem domain Ω and r_l is the positions of point excitation sources; r_l are placed on one mean free path of photon transport beneath the surface of Ω , and here we assume they are isotropic points. Subscripts x and m denote the excitation and emission wavelengths respectively. $\mu_{ax,am}$ and $\mu_{sx,sm}$ denote the absorption and scattering coefficients; $D_{x,m} = 1/3 (\mu_{ax,am} + (1-g)\mu_{sx,sm})$ denotes the diffusion coefficient. Θ is the excitation intensity and $\Phi(r)$ is the photon flux density at node r . $\eta \mu_{af}(r)$ is the fluorophore distribution to be reconstructed where η is the quantum yield, and q denotes the optical reflective index.

Equation (1) can be solved by finite element method through discretizing the domain with finite element meshes and it can be linearized to the following equations:

$$K_x \Phi_x = S_x \quad (2)$$

$$K_m \Phi_m = G X \quad (3)$$

Where K_x and K_m denote the system matrices of the excitation and emission propagation; and S_x is the discrete excitation source. Discretizing the unknown fluorescent target, we can get the matrix $G(i, j) = \int_{\Omega} \Phi_x(r) \varphi_i(r) \varphi_j(r) dr$, where $\varphi_i(r)$ and $\varphi_j(r)$ denote the base functions for node i and j , while vector X denotes reconstructed target. Since K_m is symmetrical and positive matrix [32], (3) can be formulated into the following Matrix-form equation:

$$\Phi_m = K_m^{-1} G X = D X \quad (4)$$

By removing the immeasurable entries in Φ_m and the corresponding rows in D , we obtain

$$\Phi_m^{meas} = AX \quad (5)$$

The matrix A , of size $N_{data} \times N_{voxels}$, is ill-posed, causing difficulties in the following reconstruction. $\Phi_m^{meas} \in R^{\{N_{data} \times 1\}}$ is the measure vector and $X \in R^{\{N_{voxels} \times 1\}}$ is vector to be solved. N_{data} is the measurements number, and N_{voxels} is the number of finite element nodes. Derivation details can be found in [10], [11], [13], and [16].

As described above, the linear relationship between the fluorescent sources inside the tissue and the surface photon density has been established. Due to the ill-posedness of the inverse problem, the direct solution does not exist. So *a priori* information such as sparsity term is proposed to obtain the acceptable approximate solution. The L1 regularization method is introduced to FMT reconstruction and (5) is expressed as the regularized least squares equation:

$$\min E(X) = \frac{1}{2} \|AX - \Phi_m^{meas}\|_2^2 + \lambda \|X\|_1 \quad (6)$$

where E denotes the objective function, λ is the regularization parameter used to balance the influence between the fidelity term and the regularization term. We can regard the columns of A as a set of base vectors and X is the coefficient vector. FMT sparse reconstruction can be considered to be the selection of as few base vectors as possible, so that the vector Φ_m^{meas} is represented by a linear combination of these base vectors, and the coefficients of these base vectors represent the unknown fluorescence source distribution. So FMT reconstruction can be seen as a basis pursuit problem, with the following form:

$$\min \|X\|_1 \text{ subject to } AX = \Phi_m^{meas} \quad (7)$$

B. Reconstruction Based on Sparsity Adaptive Correntropy Matching Pursuit

In this section, we proposed a robust SACMP method along with the HQ optimization algorithm for the FMT reconstruction.

1) Correntropy Induced Metric: For SACMP, CIM is used to evaluate the residual during the iteration. Here correntropy [27] is used to measure the similarity of two variables and it is constructed as follows

$$V(Z, Y) = E[\kappa_\sigma(Z - Y)] = \iint \kappa_\sigma(Z - Y) p_{ZY}(z, y) dz dy \quad (8)$$

where $p_{ZY}(z, y)$ denotes the joint probability density function (PDF) of Z and Y , $\kappa_\sigma(t)$ denotes Gaussian kernel with bandwidth σ shown as

$$\kappa_\sigma(t) = \frac{1}{\sqrt{2\pi}\sigma} \exp\left(-t^2/2\sigma^2\right), \quad t \in \mathbb{R} \quad (9)$$

In practical, we usually do not know the PDF of Z and Y and only some samples $\{(z_i, y_i)\}_{i=1}^m$ are available, m denotes the number of samples. So the correntropy is estimated using the samples by the formula shown as

$$\hat{V}(Z, Y) = \frac{1}{m} \sum_{i=1}^m \kappa_\sigma(z_i - y_i) \quad (10)$$

Extended to vectors $\mathbf{v}_1, \mathbf{v}_2 \in \mathbb{R}^m$, the CIM [27] is defined as

$$\begin{aligned} CIM(\mathbf{v}_1, \mathbf{v}_2) &= \left(\kappa_\sigma(0) - \hat{V}(\mathbf{v}_1, \mathbf{v}_2) \right)^{\frac{1}{2}} \\ &= C \left(\sum_{i=1}^m (1 - g_\sigma(v_1(i) - v_2(i))) \right)^{\frac{1}{2}} \end{aligned} \quad (11)$$

with $g_\sigma(t) = \exp(-t^2/2\sigma^2)$, $t \in \mathbb{R}$ and $C = \sqrt{\left(1/\left(\sqrt{2\pi}\sigma m\right)\right)} \cdot C$ is a constant which is independent of \mathbf{v}_1 and \mathbf{v}_2 . So CIM-based loss function can be defined as follows

$$L_\sigma(\mathbf{e}) := \frac{1}{m} \sum_{i=1}^m \ell_\sigma(e_i) := \frac{1}{m} \sum_{i=1}^m \sigma^2 (1 - g_\sigma(e_i)) \quad (12)$$

where $\mathbf{e} = [e_1, e_2, \dots, e_m] \in \mathbb{R}^m$ is the error vector. When \mathbf{e} is very small, above equation can be written

$$\ell_\sigma(e_i) = \sigma^2 (1 - g_\sigma(e_i)) = e_i^2 + o(e_i^2) \quad (13)$$

where $o(e_i^2)$ represents a function which is close to zero faster than e_i^2 when $e_i \rightarrow 0$. Under this circumstance, (13) is approximate to MSE criterion. The large impulsive noise will cause fast increase of MSE and accordingly severely influence the performance of the whole algorithm. In contrast, CIM-based loss function grows slowly and the upper bound of the loss function is σ^2 . So the method based on CIM is more robust in processing measurements with impulsive noise and outliers than the methods based on MSE [27].

2) Sparsity Adaptive Correntropy Matching Pursuit: Based on above CIM-based loss function, SACMP method is proposed in the framework of conventional matching pursuit. First, the initial residual is set as $r_0 = y$ and the index set is initialized as $\Lambda_0 = \emptyset$, \emptyset is a null set. In each subsequent iteration, we select some column vectors of matrix A that most correlated with the current residual as the candidate atoms. Then we solve the CIM minimization problem to get a new approximation solution as follows

$$X_k = \arg \min_{X \in \mathbb{R}^n, \sup p(X) \subset \Lambda_k} L_\sigma(y - AX) \quad (14)$$

In order to solve (14), we designed the optimization algorithm based on half-quadratic (HQ) theory [31]. Because $\ell_\sigma(e_i)$ is a convex function, (14) can be solved using some other optimization methods such as fixed point and gradient descent methods. However, the HQ optimization has special advantages for our problem. In addition to the approximate solution X_k , we can also get the weight vector w_k which indicates the entries importance of the measurement vector y . In each subsequent iteration, the weight matrix is modified to further improve the performance of SACMP in terms of robustness and accuracy. According to the convex optimization theory [33], we can obtained a convex function $\phi(s)$, $s \in \mathbb{R}$ for $g_\sigma(t) = \exp(-t^2/2\sigma^2)$ which has the following form

$$g_\sigma(t) = \sup \left\{ \frac{st^2}{\sigma^2} - \phi(s), s \in \mathbb{R}_- \right\} \quad (15)$$

$g_\sigma(t)$ reach to supremum at $s = -g_\sigma(t)$, then both sides of (15) multiplied by $-\sigma^2$ at the same time. After denoting

$r = -s$ and defining function $\psi(r) := \sigma^2 \phi(-r)$, we can get the following equation

$$-\sigma^2 g_\sigma(t) = \inf \left\{ rt^2 + \psi(r), r \in \mathbb{R}_+ \right\} \quad (16)$$

$g_\sigma(t)$ reach to infimum at $r = g_\sigma(t)$. Substituting (16) into (14), deleting the constants and reorganizing the equation simply, (14) is transformed into the form

$$\begin{aligned} \min_{X \in \mathbb{R}^n, w \in \mathbb{R}_+^m} J(X, w) &= \left\| \sqrt{\text{diag}(w)} (y - AX) \right\|_2^2 \\ \sup p(X) \subset \Lambda_k & \\ &+ \sum_{i=1}^m \psi(w(i)) \quad (17) \end{aligned}$$

where $\text{diag}(w)$ is a diagonal square matrix consisting of elements of vector w on the main diagonal. According to the HQ theory [31], (17) can be solved by the following iteration process

$$\hat{y} = AX^{(t)}$$

$$\sigma^{(t+1)} = \left(\frac{1}{2m} \|y - \hat{y}\|_2^2 \right)^{\frac{1}{2}} \quad (18)$$

$$w^{(t+1)}(i) = g_\sigma(y(i) - \hat{y}(i)), \quad i = 1, 2, \dots, m \quad (19)$$

$$X^{(t+1)} = \arg \min_{X \in \mathbb{R}^n, \sup p(X) \subset \Lambda_k} \left\| \sqrt{\text{diag}(w^{(t+1)})} (y - AX) \right\|_2^2 \quad (20)$$

where t denotes the number of iterations. From (18), the kernel size is automatically updated in the iteration process. According to (16) and (20), the algorithm is bound to converge after finite number of iterations [31]. In theory, (20) is a weighted least squares problem and the solution can be represented by the following form:

$$X^{(t+1)}|_{\Lambda_k} = \left(A^T \text{diag}(w^{(t+1)}) A \right)^{-1} A^T \text{diag}(w^{(t+1)}) y \quad (21)$$

and $X^{(t+1)}|_{\Lambda_k^c} = \mathbf{0}$, Λ_k^c is the complementary set, $X^{(t+1)}$ is solved in the set Λ_k , the elements in the vector corresponding to the set Λ_k are nonzero and the rest are zero. We will get the solutions X_k and w_k of (17) according to above methods. It is worth mentioning that the weight vector represents the degree of noise interference for measurement vector elements. When some elements are heavily contaminated by noise, the corresponding weights decrease dramatically to suppress the effect of noise. Based on this, we update the residual in the following form:

$$r_k = \sqrt{\text{diag}(w_k)} (y - AX_k) \quad (22)$$

The sparse vector is finally calculated until the cut-off conditions are satisfied. We summarize the complete procedure of the proposed method in Algorithm 1.

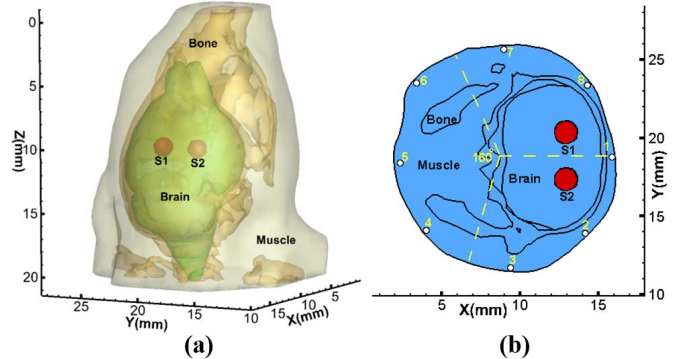


Fig. 1. The views of the heterogeneous mouse for numerical simulation studies. (a) and (b) is the 3-D and axial sectional views of the model respectively. Two simulated target source 1 (S1) and source 2 (S2) are implanted inside the brain and the centers of two sources are both in the $z = 9.5$ mm plane.

C. The Evaluation Index

To quantify the reconstruction performance, position error (PE) and relative intensity error (RIE) were calculated in the dual-source simulation experiments to measure the distance variation and intensity variation between the reconstructed region and real region, and Dice index was calculated in *in vivo* stem cell distribution experiments in order to measure the reconstruction accuracy of distribution shape.

The define of PE and RIE are given by

$$\text{PE} = \|P_r - P_0\|_2 \quad (23)$$

$$\text{RIE} = \frac{|I_r - I_0|}{I_0} \quad (24)$$

where P_r and P_0 are the center coordinates of reconstructed and actual fluorescent sources respectively, I_r denotes the maximum fluorescence yield of reconstructed sources and I_0 denotes the actual fluorescence yield of sources. Dice index is adopted to measure the shape similarity between two objects:

$$\text{Dice} = \frac{2|X \cap Y|}{|X| + |Y|} \quad (25)$$

where X and Y are the reconstructed region and true region. The degree of similarity between them gradually increases when Dice value ranges from 0 to 1.

III. EXPERIMENTS AND RESULTS

In this section, we designed the numerical simulation studies and *in vivo* stem cell distribution studies to analyze the FMT reconstruction performance of SACMP method and made a comparison with StOMP and SASP methods in terms of accuracy, stability and practicability. All the MATLAB programs ran on desktop computer with Intel(R) Core(TM) i7-6700 CPU (3.40 GHz) and 16GB RAM.

A. Numerical Simulation Study

The numerical simulation studies were first used to assess the performance of the proposed method and the Digimouse atlas [34] was used to construct the heterogeneous simulation model. The simulation model is shown in Fig. 1a, including

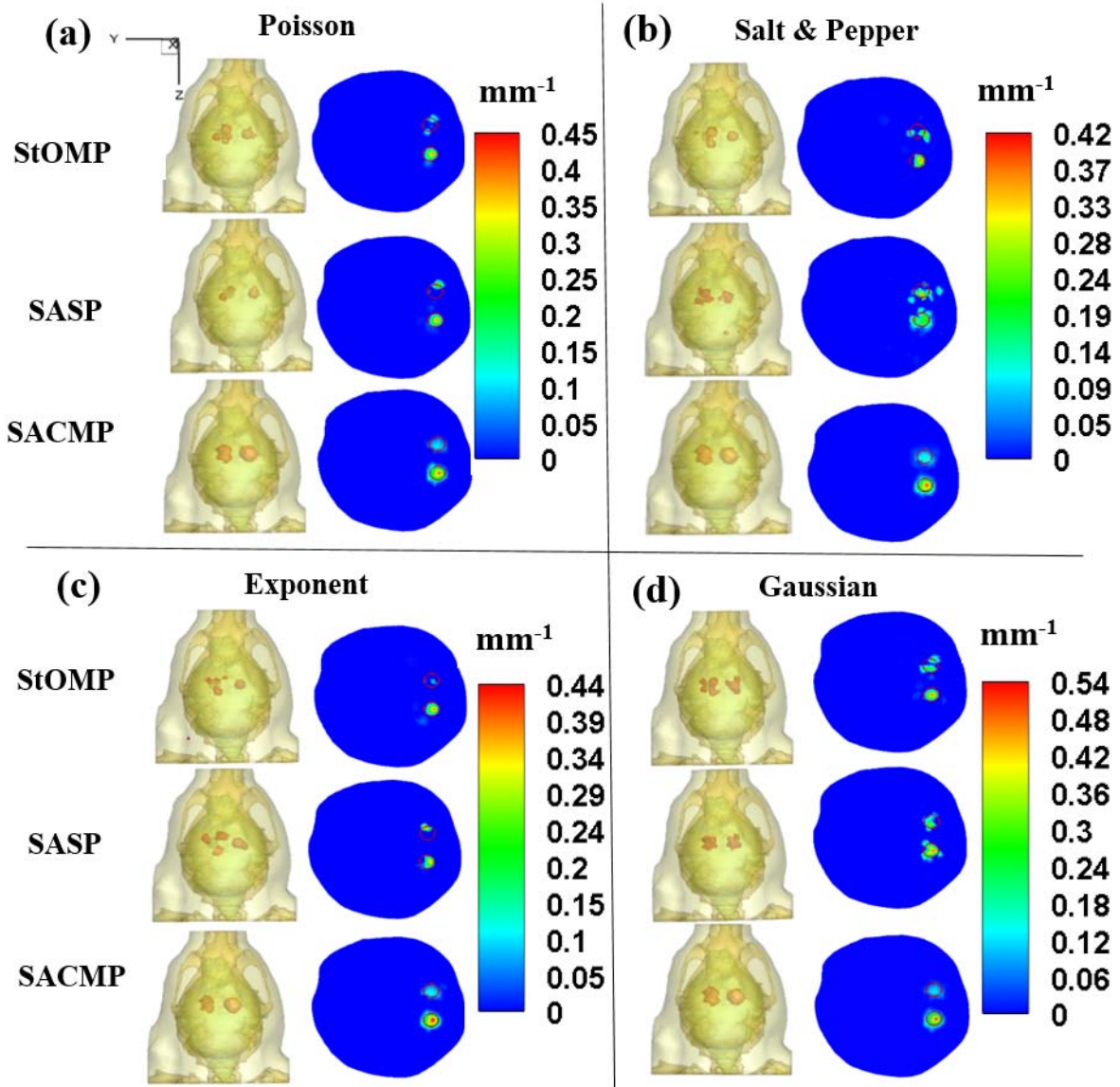


Fig. 2. The reconstruction results of the numerical simulation studies. (a) - (d) are the 3D rendering and axial slices of the reconstructed tumor sources with the data adding 15% Poisson, Salt & Pepper, Exponent, and Gaussian noise of StOMP, SASP and SACMP methods respectively. Red circle: two real sources region.

three different organs: muscle, bone and brain. Two fluorescence sources S1 and S2 with 2 mm diameters were implanted into the brain. After combining different organs, the digital mouse was meshed as 8152 nodes and 43114 tetrahedral elements in the forward process. And the phantom was discretized to 7832 nodes and 41235 tetrahedrons after simple mapping between nodes in the inverse process. The excitation and emission fluorescence wavelengths are set as 680 nm and 750 nm respectively. The optical absorption and scattering parameters of the three organs were given in Table 1 [35]. The white dot in Fig. 1b were the isotropic point excitation light sources which were located in one mean optical free path from the surface in the $z = 9.5$ mm plane. During each excitation, we acquired the surface fluorescence signal within 160 degree area from the opposite side of excitation light source (shown in Fig. 1b). After eight times of excitations, we can obtain eight measure

TABLE I
OPTICAL ABSORPTION AND SCATTERING COEFFICIENTS
(UNITS OF μ_a AND μ_s : mm^{-1})

Tissue	μ_{ax}	μ_{sx}	μ_{am}	μ_{sm}
Muscle	0.0474	0.3122	0.0287	0.2427
Bone	0.0326	2.1140	0.0197	1.8541
Brain	0.0226	1.1665	0.0167	0.8856

data sets to reduce the ill-posedness of the FMT inverse problem.

The parameters α and P_{\max} of StOMP method were set as 0.8 and 100, which were same as the values used in [21]. For SASP method, according to [23], the threshold ε and the maximum iteration number N_{\max} were set as $0.07 \times \text{norm}(y)$ and 25, where $\text{norm}(y)$ denoted the Euclidean length of

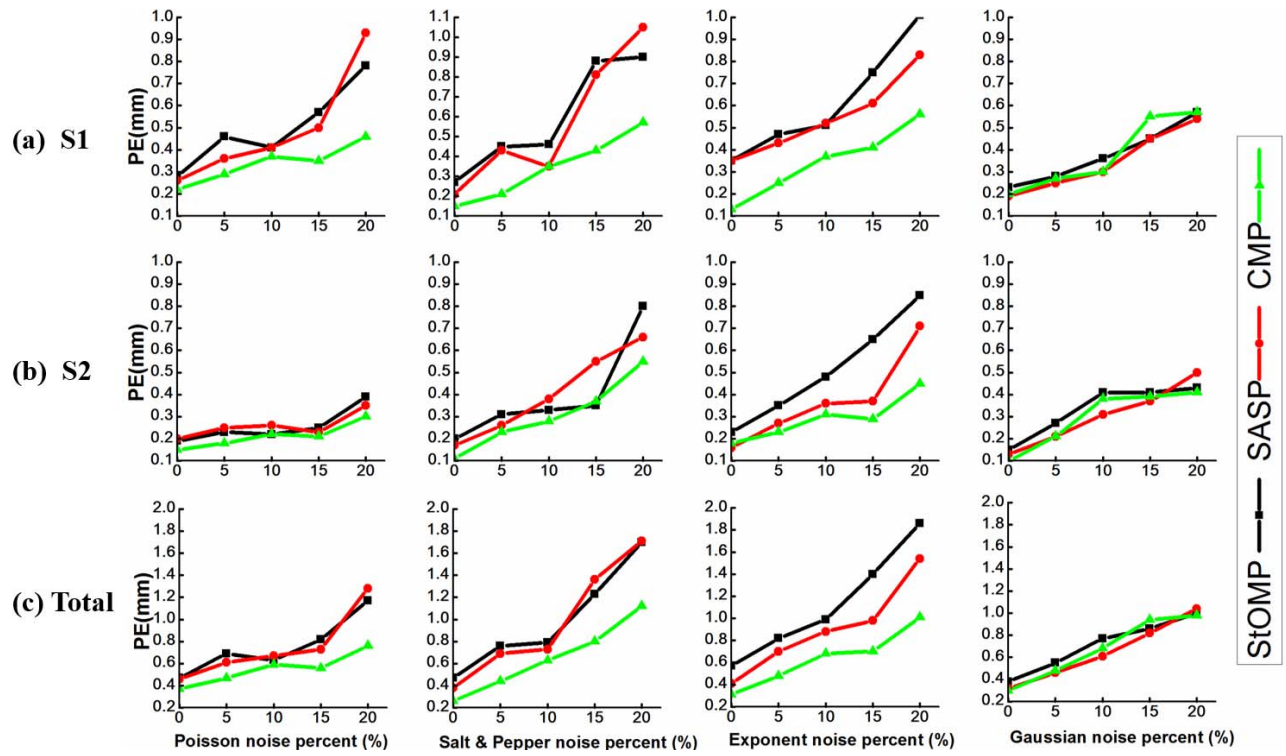


Fig. 3. Quantitative comparisons of PE in the numerical simulation experiments. (a) PEs of three methods regarding to the noise level and type for S1. (b) The same comparisons for S2. (c) The dual-source total PE of each method in different noise levels and types.

the observation vector y . In the proposed method, we ended the iteration when the residual r_k is smaller than a certain threshold ε or the iteration number reaches to maximum N_{\max} . In the experiments, the parameters ε and N_{\max} were optimized according to the experimental experience. The high noise level will cause serious calculation error and the threshold values should be adjusted accordingly. We empirically set the threshold ε as $(0.02, 0.05, 0.07, 0.1, 0.13) \times \text{norm}(y)$ for the 0%, 5%, 10%, 15% and 20% noise tests. In our experiments, we can obtain satisfactory results using the proposed method under these threshold values. The maximum iteration number N_{\max} was set as 30 and each of reconstruction processes using our method stopped within 30 iterations.

Fig. 2 demonstrates the reconstruction results of StOMP, SASP and SACMP methods with the measure data adding 15% Poisson, Salt & Pepper, Exponent and Gaussian noise respectively. The 3D rendering and the axial slice crossing the centers of two fluorescent sources ($Z = 9.5$ mm) are illustrated for each method in different noise types. Compared with StOMP and SASP methods, SACMP provides the best performance with the smallest PE and RIE in the tests of four different types of noise. These superiorities of SACMP are more obvious in the test of non-Gaussian noise.

The quantitative comparisons of PEs in Fig. 3 further confirm these observations. The real fluorescence position centers of S1 and S2 are $(13.1, 20.5, 9.5$ mm) and $(13.1, 17.0, 9.5$ mm). For S1, SACMP achieves much smaller PEs for the test of non-Gaussian noise and the similar performance for the test of Gaussian noise (Fig. 3a). For S2, the PEs of SACMP are smaller than that of the other two methods (Fig. 3b).

After combining the PEs of S1 and S2, the PEs derived from SACMP are greatly smaller than that obtained by conventional StOMP and SASP methods except for the tests of Gaussian noise (Fig. 3c). The results showed that SACMP significantly improve the reconstruction accuracy when the measurements contaminated by non-Gaussian noise ($P < 0.05$ for SACMP vs StOMP or SASP).

The quantitative comparisons of RIEs for each method with different types and levels of noise are shown in Fig. 4. The actual fluorescence yields of S1 and S2 are both set as 0.8 mm^{-1} . Fig. 4a demonstrates that the RIEs of SACMP are smaller than that given by the rest of methods on dealing with the four types of noise. For S2, the RIEs of SACMP and SASP are similar when data is added Exponent and Gaussian noise (Fig. 4b). Overall speaking, the SACMP achieve the most accurate performance in term of RIE for different levels and types of noise. The PE and RIE of reconstruction results showed that the SACMP method has the highest accuracy and robustness on handling with both Gaussian and non-Gaussian noise issue.

Fig. 5 demonstrates the performance of SACMP in the double-source phantom experiments with different number of mesh nodes (Fig. 5a) and different step sizes (Fig. 5b). Obviously, large number of node will produce more accurate reconstruction result, but the amount of computation will increase rapidly. Both PE and RIE are better when the number of nodes increases, while the performance keep relatively stable as the node number reach more than 7832.

In the step sizes test, the reconstruction results with different step sizes from 1 to 5 are demonstrated in Fig. 5b. The

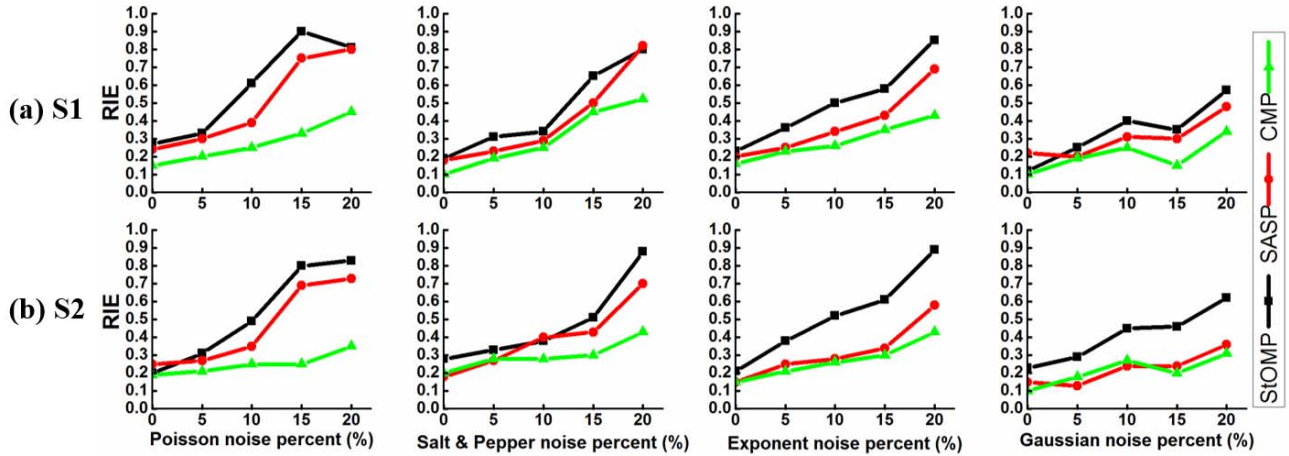


Fig. 4. Quantitative comparisons of RIE in the numerical simulation experiments. (a) RIE of three methods regarding to the different levels and types of noise for S1. (b) The same comparisons for S2.

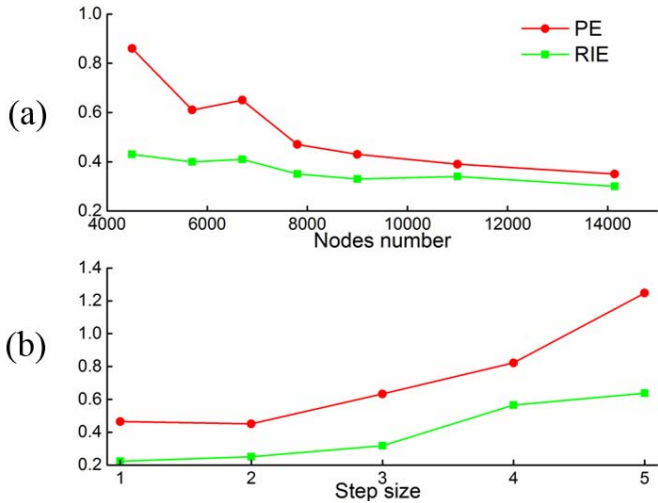


Fig. 5. Quantitative comparisons of the parameters test with PE (red) and RIE (green). (a) The nodes density test. (b) The step size test.

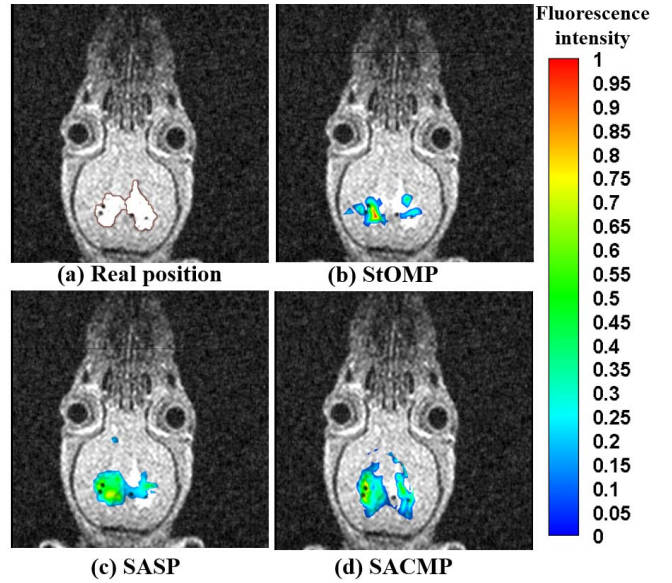


Fig. 7. The real position of fluorescence source in brain and the reconstruction results of the StOMP, SASP and SACMP methods. The area surrounded by brown curve is the real position and the colorbar is normalized. (a) The rainbow color superimposed on MR image slices are the reconstructed results (b, c, d).

B. In Vivo Experiment

To further evaluate the practical performance of the SACMP algorithm, we carried out *in vivo* mesenchymal stem cells (MSCs) distribution experiments in brain. In this work, the MSCs were incubated with the multimode biological probe for two hours before transplantation [36]. The excitation and emission fluorescence wavelengths of probe are 680 nm and 750 nm respectively. The female nude mice (6 weeks) were purchased from Peking University Laboratory Animal Center. Then we build a traumatic brain injury animal model in the left hemisphere and the labeled stem cells were injected into the contralateral hemisphere subsequently [37]. 7 days post injection, some MSCs migrated to the contralateral hemisphere injury area, and the fluorescence images of the multimodal probe and CT anatomical data were collected using the multimodal imaging system developed by our group [38], then

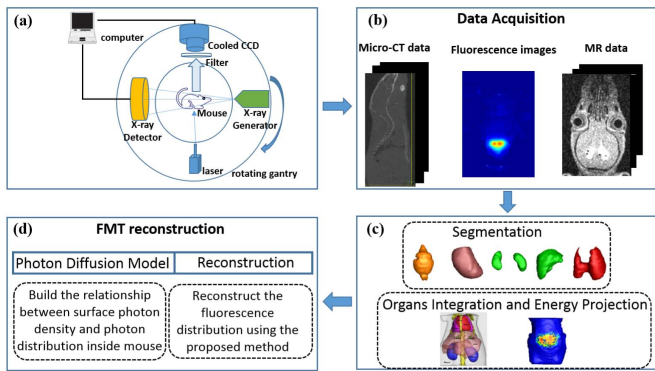


Fig. 6. The data processing scheme of the FMT based on multi-modality imaging system.

figure shows that the PE and RIE increase while the step size changes from $S = 1$ to $S = 5$. A smaller step size will achieve higher reconstruction accuracy. Correspondingly, the number of iterations will increase significantly. Without decreasing reconstruction accuracy severely, we set step size as 2 with the consideration of the reconstruction efficiency.

Algorithm 1 SACMP

Input: matrix A , vector y and stopping criterions (threshold ε and the maximum number of iterations N_{\max}).

Output: an estimate solution \hat{X} and weight vector \hat{w} of FMT problem.

Initialization: the residual $r_0 = y$, the index set $\Lambda_0 = \emptyset$, the iterator number $k = 0$, step size $S = 2$, sparsity factor $K = S$.

while $r_k > \varepsilon$ and $k < N_{\max}$ **do**

1: $k = k + 1$;

2: **selection.** In matrix A , select K columns which are most correlated with the residual

$$\lambda_k = \arg \max_{i=1,2,\dots,n} |\langle r_{k-1}, a_i \rangle|$$

3: **Amplification.** Add the selected columns to the index set

$$\Lambda_k = \Lambda_{k-1} \cup \{\lambda_k\}$$

4: **Estimation.** The CIM minimization problem is solved according to the formulas

$$w^{(t+1)}(i) = g_\sigma(y(i) - (AX^t)(i)), \quad i = 1, 2, \dots, m$$

$$X^{(t+1)} = \arg \min_{X \in \mathbb{R}^n, \sup p(X) \subset \Lambda_k} \left\| \sqrt{\text{diag}(w^{(t+1)})} (y - AX) \right\|_2^2$$

5: **Update the residual.**

$$r_k = \sqrt{\text{diag}(w_k)} (y - AX_k)$$

6: **Update the sparsity factor K .**

if $r_k > r_{k-1}$ then

$$K = K + S, \quad r_k = r_{k-1}, \quad \Lambda_k = \Lambda_{k-1}$$

end if

end while

Output: The sparse solution $\hat{X} = X_k$ and the weight vector $\hat{w} = w_k$.

the MR signals of the multimodal probe was acquired by the small animal magnetic resonance imaging system (1.5t, M3TM, Aspect Imaging, Israel). All animal experiments were performed under the guidelines approved by the Institutional Animal Care and Use Committee (IACUC) at Peking University, and we have tried our best to alleviate the suffering of animals. During the data acquisition, the mice were anesthetized by isoflurane-oxygen mixed gas (500 ml/min, Matrx VMR Small Animal Anesthesia Machine, Matrx, USA).

The fluorescence images were acquired by an electron multiplying charge coupled device (EMCCD) camera (iXonEM+888, ANDOR, UK) with 5 seconds exposure and binning 4 using 750 ± 10 nm bandpass filter. The anatomical structures including muscle, bone and brain were acquired and their optical parameters were listed in Table 1 [27]. Then the semi-segmented organs were discretized into finite element meshes and the surface fluorescence density was mapped onto these meshes. The MR images were acquired with the parameters: TR 6000 ms, TE 50 ms, slice thickness 0.5 mm, and slice spacing 0.2 mm. The MR signals of the probe can be

received as the actual distribution of stem cells, so we can use it to evaluate the performance of our reconstruction method. It should be pointed out that the head of mouse can be regarded as rigid object which is benefit to registration between CT and MR data [39]. Fig. 4 shows the whole data processing scheme of *in vivo* experiment.

The area depicted by brown curve is considered to be the real distribution of stem cells (Fig. 5a). The figure shows that the reconstructed result based on SACMP match best with the real fluorescence area in shape and position among all the three methods. The Dice index of the SACMP, SASP and StOMP methods for this experiment are 0.78, 0.55 and 0.31 respectively. The results indicate that the SACMP method has considerable application prospect for brain stem cell distribution experiments.

IV. DISCUSSION AND CONCLUSION

In this paper, we proposed a SACMP reconstruction method to non-invasively detect the transplanted stem cells in brain. The biggest superiority of SACMP is that the sensitivity to non-Gaussian noise of the conventional MP method is successfully overcome, thus the location and distribution shape of stem cell are accurately reconstructed. This is achieved by using CIM criterion instead of MSE criterion of the residual in the iteration of algorithm, then HQ optimization algorithm is used to minimize the CIM and calculate the weight vector to improve the accuracy of the selected atoms.

Simulation studies demonstrated that the reconstruction results of SACMP method had better performance than StOMP and SASP methods on dealing with data contaminated by non-Gaussian noise. And the three methods have similar performance on measurements when the noise obey the Gaussian distribution. The experimental results are consistent with our theoretical description of it in section II. With the non-Gaussian noise increasing, the superiority of our method over the other two methods is more obvious. It is worth noting that even we add 20% noise to the data, the method still have acceptable results.

To further evaluate the practicability of SACMP method, the FMT reconstruction results of the *in vivo* stem cells distribution in traumatic brain injury mice were obtained and the MRI images of the multimodal probe were used as the reference of evaluation. The reconstructed result of SACMP had the biggest Dice index which means the reconstructed stem cell distribution shape match better with the actual morphology. To the best of our knowledge, this is the first study that acquired such accurate and robust FMT reconstruction of stem cell distribution in mice brain.

For *in vivo* stem cell distribution problem, the fluorescent source in animal body is weak which can be easily disturbed by all kind of noise, for example external interference light, excitation light and so on. Meanwhile, the CCD camera will generate photon noise, dark current noise and read noise during the image acquisition. The noise distribution of measure data is so complex that Gaussian distribution approximation will not represent it accurately and this will necessarily introduce serious error. Robustness of SACMP to noise makes it more suitable for stem cells distribution problems. The *in vivo*

experiment results also demonstrated that our method had better performance than the other two conventional MP methods.

However, during an iteration, the number of selected atoms will affect the stability of the weight vector, but the mechanism is not yet clearly clarified. One of our future work will focus on proposing proper methods to reduce the limitation. Another potential avenue would be the promotion of application of CIM in algorithms which use the MSE criterion.

In conclusion, we proposed a SACMP method for the inverse problem of FMT. Comparing with the conventional MP methods, it had better performance in terms of accuracy, robustness and practicability. This enabled FMT more feasible and effective for stem cell distribution in practical mice brain injury models.

ACKNOWLEDGMENT

The authors would like to thank Jing Li (Cnkingbio Company Ltd, Beijing, China), Hongyan Yin, and Jining Liu for biotechnical support (Stem cells). They also would like to thank Yuan Gao and Hongbo Guo for the assistance of *in vivo* experiment.

REFERENCES

- [1] G. Chen, F. Tian, Y. Zhang, Y. Zhang, C. Li, and Q. Wang, "Tracking of transplanted human mesenchymal stem cells in living mice using near-infrared Ag₂S quantum dots," *Adv. Funct. Mater.*, vol. 24, no. 17, pp. 2481–2488, 2014.
- [2] T.-J. Wu *et al.*, "Tracking the engraftment and regenerative capabilities of transplanted lung stem cells using fluorescent nanodiamonds," *Nature Nanotechnol.*, vol. 8, no. 9, pp. 682–689, 2013.
- [3] G. Feng *et al.*, "Ultrabright organic dots with aggregation-induced emission characteristics for cell tracking," *Biomaterials*, vol. 35, no. 30, pp. 8669–8677, 2014.
- [4] S. Huang *et al.*, "Highly fluorescent and bioresorbable polymeric nanoparticles with enhanced photostability for cell imaging," *Nanoscale*, vol. 7, no. 3, pp. 889–895, 2015.
- [5] Y. Wu *et al.*, "Functional quantum dot-siRNA nanoplexes to regulate chondrogenic differentiation of mesenchymal stem cells," *Acta Biomaterialia*, vol. 46, pp. 165–176, Dec. 2016.
- [6] A. Ale, V. Ermolayev, E. Herzog, C. Cohrs, M. H. De Angelis, and V. Ntziachristos, "FMT-XCT: *In vivo* animal studies with hybrid fluorescence molecular tomography–X-ray computed tomography," *Nature methods*, vol. 9, no. 6, pp. 615–620, 2012.
- [7] Y. An *et al.*, "A novel region reconstruction method for fluorescence molecular tomography," *IEEE Trans. Biomed. Eng.*, vol. 62, no. 7, pp. 1818–1826, Jul. 2015.
- [8] W. Bangerth and A. Joshi, "Adaptive finite element methods for the solution of inverse problems in optical tomography," *Inverse Problems*, vol. 24, no. 3, p. 034011, 2008.
- [9] N. Cao, A. Nehorai, and M. Jacob, "Image reconstruction for diffuse optical tomography using sparsity regularization and expectation–maximization algorithm," *Opt. Exp.*, vol. 15, no. 21, pp. 13695–13708, 2007.
- [10] X. Song, D. Wang, N. Chen, J. Bai, and H. Wang, "Reconstruction for free-space fluorescence tomography using a novel hybrid adaptive finite element algorithm," *Opt. Exp.*, vol. 15, no. 26, pp. 18300–18317, 2007.
- [11] D. Wang, X. Liu, Y. Chen, and J. Bai, "A novel finite-element-based algorithm for fluorescence molecular tomography of heterogeneous media," *IEEE Trans. Inf. Technol. Biomed.*, vol. 13, no. 5, pp. 766–773, Sep. 2009.
- [12] X. Ma *et al.*, "Enhanced immunotherapy of SM5-1 in hepatocellular carcinoma by conjugating with gold nanoparticles and its *in vivo* bioluminescence tomographic evaluation," *Biomaterials*, vol. 87, pp. 46–56, May 2016.
- [13] V. Ntziachristos, "Fluorescence molecular imaging," *Annu. Rev. Biomed. Eng.*, vol. 8, pp. 1–33, 2006.
- [14] M. T. Berninger *et al.*, "Fluorescence molecular tomography of DiR-labeled mesenchymal stem cell implants for osteochondral defect repair in rabbit knees," *Eur. Radiol.*, vol. 27, no. 3, pp. 1105–1113, 2016.
- [15] I. S. Behbahan, A. Keating, and R. P. Gale, "Concise review: Bone marrow autotransplants for liver disease?" *Stem Cells*, vol. 31, no. 11, pp. 2313–2329, Nov. 2013.
- [16] A. X. Cong and G. Wang, "A finite-element-based reconstruction method for 3D fluorescence tomography," *Opt. Exp.*, vol. 13, no. 24, pp. 9847–9857, 2005.
- [17] V. Ntziachristos, "Going deeper than microscopy: The optical imaging frontier in biology," *Nature Methods*, vol. 7, no. 8, pp. 603–614, 2010.
- [18] P. Mohajerani, A. A. Eftekhari, J. Huang, and A. Adibi, "Optimal sparse solution for fluorescent diffuse optical tomography: Theory and phantom experimental results," *Appl. Opt.*, vol. 46, no. 10, pp. 1679–1685, 2007.
- [19] D. Han *et al.*, "Sparsity-promoting tomographic fluorescence imaging with simplified spherical harmonics approximation," *IEEE Trans. Biomed. Eng.*, vol. 57, no. 10, pp. 2564–2567, Oct. 2010.
- [20] D. Han *et al.*, "A fast reconstruction algorithm for fluorescence molecular tomography with sparsity regularization," *Opt. Exp.*, vol. 18, pp. 8630–8646, Apr. 2010.
- [21] D. Han *et al.*, "Efficient reconstruction method for L1 regularization in fluorescence molecular tomography," *Appl. Opt.*, vol. 49, no. 36, pp. 6930–6937, 2010.
- [22] J. Ye, Y. Du, Y. An, C. Chi, and J. Tian, "Reconstruction of fluorescence molecular tomography via a nonmonotone spectral projected gradient pursuit method," *J. Biomed. Opt.*, vol. 19, no. 12, p. 126013, 2014.
- [23] J. Ye *et al.*, "Fast and robust reconstruction for fluorescence molecular tomography via a sparsity adaptive subspace pursuit method," *Biomed. Opt. Exp.*, vol. 5, no. 2, pp. 387–406, 2014.
- [24] M. Elad, B. Matalon, and M. Zibulevsky, "Coordinate and subspace optimization methods for linear least squares with non-quadratic regularization," *Appl. Comput. Harmonic Anal.*, vol. 23, no. 3, pp. 346–367, 2007.
- [25] V. C. Kavuri, Z.-J. Lin, F. Tian, and H. Liu, "Sparsity enhanced spatial resolution and depth localization in diffuse optical tomography," *Biomed. Opt. Exp.*, vol. 3, no. 5, pp. 943–957, 2012.
- [26] D. Erdogmus and J. C. Principe, "An error-entropy minimization algorithm for supervised training of nonlinear adaptive systems," *IEEE Trans. Signal Process.*, vol. 50, no. 7, pp. 1780–1786, Jul. 2002.
- [27] W. Liu, P. P. Pokharel, and J. C. Principe, "Correntropy: Properties and applications in non-Gaussian signal processing," *IEEE Trans. Signal Process.*, vol. 55, no. 11, pp. 5286–5298, Nov. 2007.
- [28] Y. Feng, X. Huang, L. Shi, Y. Yang, and J. A. K. Suykens, "Learning with the maximum correntropy criterion induced losses for regression," *J. Mach. Learn. Res.*, vol. 16, pp. 993–1034, 2015.
- [29] D.-S. Pham and S. Venkatesh, "Improved image recovery from compressed data contaminated with impulsive noise," *IEEE Trans. Image Process.*, vol. 21, no. 1, pp. 397–405, Jan. 2012.
- [30] Y. Wang, Y. Y. Tang, and L. Li, "Correntropy matching pursuit with application to robust digit and face recognition," *IEEE Trans. Cybern.*, vol. 47, no. 6, pp. 1354–1366, Jun. 2017.
- [31] M. Nikolova and M. K. Ng, "Analysis of half-quadratic minimization methods for signal and image recovery," *SIAM J. Sci. Comput.*, vol. 27, no. 3, pp. 937–966, 2005.
- [32] C. Qin *et al.*, "Galerkin-based meshless methods for photon transport in the biological tissue," *Opt. Exp.*, vol. 16, no. 25, pp. 20317–20333, 2008.
- [33] X.-T. Yuan and B.-G. Hu, "Robust feature extraction via information theoretic learning," in *Proc. 26th Annu. Int. Conf. Mach. Learn.*, 2009, pp. 1193–1200.
- [34] B. Dogdas, D. Stout, A. F. Chatzioannou, and R. M. Leahy, "Digimouse: A 3D whole body mouse atlas from CT and cryosection data," *Phys. Med. Biol.*, vol. 52, no. 3, p. 577, 2007.
- [35] S. L. Jacques, "Optical properties of biological tissues: A review," *Phys. Med. Biol.*, vol. 58, no. 11, p. R37, 2013.
- [36] Y. Tang *et al.*, "MRI/SPECT/fluorescent tri-modal probe for evaluating the homing and therapeutic efficacy of transplanted mesenchymal stem cells in a rat ischemic stroke model," *Adv. Funct. Mater.*, vol. 25, no. 7, pp. 1024–1034, Feb. 2015.
- [37] S. F. Merkel *et al.*, "Factors affecting increased risk for substance use disorders following traumatic brain injury: What we can learn from animal models," *Neurosci. Biobehavioral Rev.*, vol. 77, pp. 209–218, Jun. 2017.
- [38] M. Liu *et al.*, "In vivo pentamodal tomographic imaging for small animals," *Biomed. Opt. Exp.*, vol. 8, no. 3, pp. 1356–1371, Mar. 2017.
- [39] F. Maes, A. Collignon, D. Vandermeulen, G. Marchal, and P. Suetens, "Multimodality image registration by maximization of mutual information," *IEEE Trans. Med. Imag.*, vol. 16, no. 2, pp. 187–198, Apr. 1997.